Lawrence Berkeley National Laboratory
Recent Work

Title
Splitter target for controlling magnetic reconnection in relativistic laser plasma interactions

Permalink
https://escholarship.org/uc/item/0sz936hn

Journal
Plasma Physics and Controlled Fusion, 60(4)

ISSN
0741-3335

Authors
Gu, YJ
Bulanov, SS
Korn, G
et al.

Publication Date
2018-03-08

DOI
10.1088/1361-6587/aab059

PAPER

Splitter target for controlling magnetic reconnection in relativistic laser plasma interactions

Splitter target for controlling magnetic reconnection in relativistic laser plasma interactions

Y J Gu[1,2] , **S S Bulanov**[3], **G Korn**[1] **and S V Bulanov**[1,4,5]

[1] Institute of Physics of the ASCR, ELI-Beamlines, Na Slovance 2, 18221 Prague, Czechia
[2] Institute of Plasma Physics of the CAS, Za Slovankou 1782/3, 18200 Prague, Czechia
[3] Lawrence Berkeley National Laboratory, Berkeley, CA 94720, United States of America
[4] Kansai Photon Research Institute, National Institutes for Quantum and Radiological Science and Technology, 8-1-7 Umemidai, Kizugawa-shi, Kyoto 619-0215, Japan
[5] A. M. Prokhorov Institute of General Physics, the Russian Academy of Sciences, Vavilova 38, 119991 Moscow, Russia

E-mail: yanjun.gu@eli-beams.eu

Abstract
The utilization of a conical target irradiated by a high power laser is proposed to study fast magnetic reconnection in relativistic plasma interactions. Such target, placed in front of the near critical density gas jet, splits the laser pulse, forming two parallel laser pulses in the 2D case and a donut shaped pulse in the 3D case. The magnetic annihilation and reconnection occur in the density downramp region of the subsequent gas jet. The magnetic field energy is converted into the particle kinetic energy. As a result, a backward accelerated electron beam is obtained as a signature of reconnection. The above mechanisms are demonstrated using particle-in-cell simulations in both 2D and 3D cases. Facilitating the synchronization of two laser beams, the proposed approach can be used in designing the corresponding experiments on studying fundamental problems of relativistic plasma physics.

Keywords: magnetic reconnection, acceleration of charged particles, relativistic laser plasmas

(Some figures may appear in colour only in the online journal)

1. Introduction

The study of different aspects of magnetic reconnection is mostly inspired by the observation of charged particle acceleration in strongly magnetized space plasmas [1–5]. The magnetic reconnection allows one to transfer the energy from the magnetic field into the charged particle energy via the strong electric field generation due to the topology change of the magnetic field. In the cases of astrophysical and laboratory plasmas, the magnetic reconnection plays a key role in a broad range of processes exemplified by solar flares [6–8], coronal mass ejections [9, 10], open and closed planetary magnetospheres [11–13], gamma-ray bursts [14–17] and nuclear fusion plasma instabilities [18–21]. Due to the recent progress in laser technology, high power lasers were employed to study the fast magnetic reconnection regime [22–27]. In fact, when a high-intensity laser pulse interacts with a plasma target the accelerated electron bunches generate strong magnetic fields with non-trivial topology. This eventually leads to the magnetic reconnection. For instance, recent experiments using intense and high-energy laser pulses showed the generation of plasma outflows with keV electrons and with plasmoid generated in current sheets formed during reconnection on the time scale of nanoseconds [28].

However, under the ultra-relativistic conditions, the magnetic field effects on the processes in collisionless plasmas become different from those in the nonrelativistic regime due to the constraint of the electric current density, i.e. the finite electron density and the electron velocity never exceeds the speed of light in vacuum. The relativistic regime of magnetic field line reconnection is called the dynamic dissipation of the magnetic field proposed by S I Syrovatskii

[29]. We recently demonstrated using 2D particle-in-cell (PIC) computer modeling that the fast relativistic magnetic annihilation can be achieved with two parallel ultra-short petawatt laser pulses co-propagating in underdense plasma target [30, 31]. The contributions from the displacement current and the induced electric field were demonstrated to be dominating the charged particle acceleration inside the current sheet. In order to study this regime experimentally one would need two laser pulses synchronized within a maximum delay of several laser periods, which is highly challenging. In order to avoid the synchronization issue, the utilization of a higher order laser mode, TEM (1, 0), was suggested in [32], and a micro-scale plasma slab, designed to the magnetic reconnection was proposed in [33].

In the present paper, we propose an approach based the target engineering. We are going to place a solid cone target in front of the near critical gas jet. A single high power laser pulse will be split by a wedge forming two parallel pulses in 2D case and by the cone leading to a donut shape pulse in 3D case. The magnetic reconnection and the backward relativistic electron acceleration are observed in both 2D and 3D PIC simulations. The results of these simulations indicate that such experiments can be performed at the upcoming laser facilities such as ELI-Beamlines. Moreover, the proposed regime of interaction can be used for formulating the program of forthcoming experiments, including the research in laboratory astrophysics [5].

2. Simulation setup

In order to demonstrate the proposed scheme, we present here the results of the kinetic simulation obtained with the relativistic electromagnetic code EPOCH [34, 35] in 2.5-dimensional configuration (two spatial and three momentum components for particles). We justify the use of the 2D simulations to model the mechanism of the magnetic reconnection by increased numerical resolution. Also the 2D configuration provides a more clear view at the evolutions of plasma density and EM fields, which are less obvious in 3D. In the next section we also present the results of 3D PIC simulations in order to compare with 2D results and illustrate the process of magnetic reconnection in a realistic setup.

The interaction modeling is set up as follows. A S-polarized Gaussian pulse with the peak intensity of 10^{21} W cm^{-2} propagating along the x-axis is focused onto a solid cone. The normalized amplitude is $a_0 = eE_0/m_e\omega c \approx 27$, where E_0 and ω are the laser electric field strength and frequency, e and m_e are the electron charge and mass, respectively; and c is the speed of light in vacuum. The pulse duration is $\tau = 15$ fs and the spot size (FWHM) is 20 λ. The laser wavelength is $\lambda = 1 \mu$m. These parameters correspond to multi petawatt laser power. The solid gold (Au) cone of thickness $L = 7 \mu$m and density $N = 30 n_c$ is placed in $15\lambda < x < 22\lambda$. Here $n_c = m_e\omega^2/4\pi e^2$ is the plasma critical density. The opening angle of the conical target is 60°. The density of the conical target is high enough to keep its main structure mostly intact during the interaction with laser pulse. Only some of the surface electrons are evacuated from the target

by the laser. The solid cone target is followed by an underdense hydrogen plasma with the peak density of $n_0 = 0.3 n_c$. The longitudinal density profile remains constant from $x = 22\lambda$ to $x = 50\lambda$. Then the plasma density decreases linearly to 0 at $x = 110\lambda$. The interaction setup is shown in figure 1(a). The simulation box has the size of 180 λ and 80 λ in the x and y direction respectively. The mesh size in the case of 2D simulation is $\delta x = \delta y = \lambda/50$. The timestep is $0.0013 T_0$, where $T_0 = 2\pi/\omega$ is the laser period. All the quasiparticles (24 per cell) are initially at rest. Open boundary conditions are applied to both fields and particles.

3. Laser pulse splitting and electron acceleration

The incident laser pulse is split into two parts by the solid cone, which is the wedge in the 2D case. Figure 1(a) shows the forward (in red) and backward (in blue) propagating components of the laser field. The normalized cross section of the scattered light is proportional to the square of the ratio between the radius of the cone and the laser spot, $(D/W_0)^2$. Since the radius of the cone target is much smaller than the laser spot size, only a small portion of the laser pulse is reflected. The black arrows show the Poynting vectors during the laser splitting. Most of the laser radiation propagates forward with a slight deflection in perpendicular direction. As shown in figure 1(b), the energy of the reflected radiation amounts to about 1% of the incident pulse energy. One can also see from this figure that the transmitted laser radiation is splitted equally between the lower and the upper half of the simulation box. Therefore, the forward radiation pattern can be identified as the twin pulses propagating parallel with perfect synchronization. After the splitting these two pulses continue to propagate in the subsequent underdense hydrogen plasma region. The power of the split laser pulse is much higher than the threshold for the relativistic self-focusing, $P > P_c n_c/n_0$, where $P_c = 2m_e^2 c^5/e^2 = 17$ GW. The electric field amplitude of the pulses is strong enough to expel the electrons and form plasma channels. The propagation of an intense laser pulse in such self-generated channel can be approximately described as the propagation of an EM wave in a waveguide [36]. The radius of plasma channel can be determined from balancing an electron energy gain in the charge separation field and in the laser field:

$$R_{ch} = \sqrt{\frac{a_{ch} n_c}{n_0}} \frac{\lambda}{\pi}, \qquad (1)$$

where a_{ch} is the amplitude of laser pulse vector potential in the channel [36]. The radius is estimated to be about 6 μm in our case, which is in good agreement with the simulation results. As the lasers propagate in the near critical density plasma, a portion of electrons is trapped behind the pulses and is accelerated by wakefields. The distribution of plasma density is shown in figure 1(c), from which one can see the laser pulses are propagating along two axes $y = \pm 6.5 \lambda$, respectively. The lineouts of the longitudinal electric fields and laser field amplitudes along these axes are plotted in
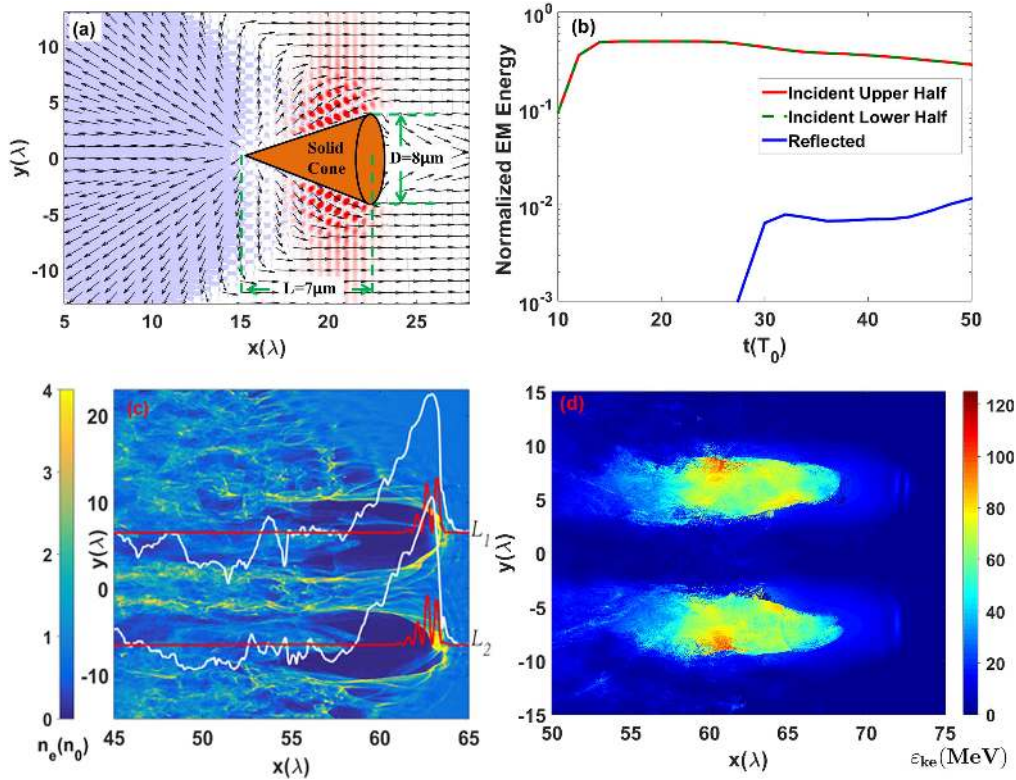
Figure 1. (a) The scheme of the cone target and the laser splitting. The red color represents forward propagating pulse and the blue is for the reflected components. The direction of the Pointing vector is shown by black arrows. (b) The evolution of the EM field energy of the incident and reflected pulses. The red and the dashed green curves correspond to the forward propagating EM field in the upper half ($y > 0$) and lower half ($y < 0$) of the simulation box, respectively. The blue line is the reflected field. (c) The twin structure of the electron plasma channel at $t = 76\,T_0$. The longitudinal electric field and the laser amplitude are represented by the white and red lines with the normalization of $(0.1\,\mathrm{GV\,cm^{-1}})$ and $0.1 \times I_0$, where I_0 is the laser peak intensity. The locations of the red lines indicate the laser axes $y = \pm 6.5\,\lambda$ and also the zero-scale lines of the laser intensity and the electric field. (d) The average kinetic energy distribution of the electrons at $t = 86\,T_0$.

white and red. The maximum amplitude of the wakefield is given as [37]

$$E_{\max} = \frac{a^2/2}{\sqrt{1 + a^2/2}} \frac{m_e \omega c}{e} \sqrt{\frac{n_0}{n_c}}. \qquad (2)$$

The strength of the electric field reaches several tens $\mathrm{GV\,cm^{-1}}$ in our case. The electrons trapped in such a strong field are accelerated to the energies exceeding 100 MeV over the distance equal to the length of the density plateau ($22\lambda < x < 50\lambda$) as shown in figure 1(d), where the kinetic energy distribution of the electrons is presented. Both the accelerated electron beams contain a large electric charge $2\,\mathrm{nC}\,\mu\mathrm{m^{-1}}$ of the relativistic electrons ($\mathcal{E}_{ke} > 1$ MeV).

4. Magnetic dipolar regions formation and annihilation

The electric currents from the accelerated beams produce azimuthal magnetic field (in the 2D case the magnetic field is directed along the z-axis). According to Ampère–Maxwell law

$$c\nabla \times \mathbf{B} = 4\pi \mathbf{j} + \partial_t \mathbf{E}, \qquad (3)$$

the amplitude of the magnetic field can be estimated by

assuming a quasistatic condition, $\partial_t \mathbf{E} = 0$. Then the magnetic field strength in terms of the channel radius is $B/R_{ch} = 4\pi n e v_e/c \approx 4\pi n e$, here we assume the electron velocity to be close to the speed of light. The electrons initially located in the volume of the plasma channel contribute to the formation of the electric current. Due to the plasma lensing effect, the continuously injected electrons are focused towards the current axis and the pinched density determines the current density, which is dominated by low energy electrons as proposed in [36]. As a result we can estimate the magnetic field strength in the channel, which is $B_z \approx 1.1$ GG and is slightly overestimated compared to the results of simulations. It is most probably due to the decrease of the laser power after splitting as well as the depletion of the twin laser pulses in the NCD plasma. The distribution of the magnetic field at $t = 66\,T_0$ is shown in figure 2(a), where two magnetic dipolar regions formed by the two electron beams can clearly be seen. The black curve is the profile of the magnetic field along the line $x = 50\,\lambda$. The dashed line indicate the zero value and the oscillation amplitude which is of the order of 0.6 GG. At $t = 66\,T_0$, the magnetic fields of the twin pulses are not overlapping yet and leave a non-magnetized region between the twin channels.

As it was shown in [30, 31] the magnetic quadrupole structure transversely expands when it enters the density
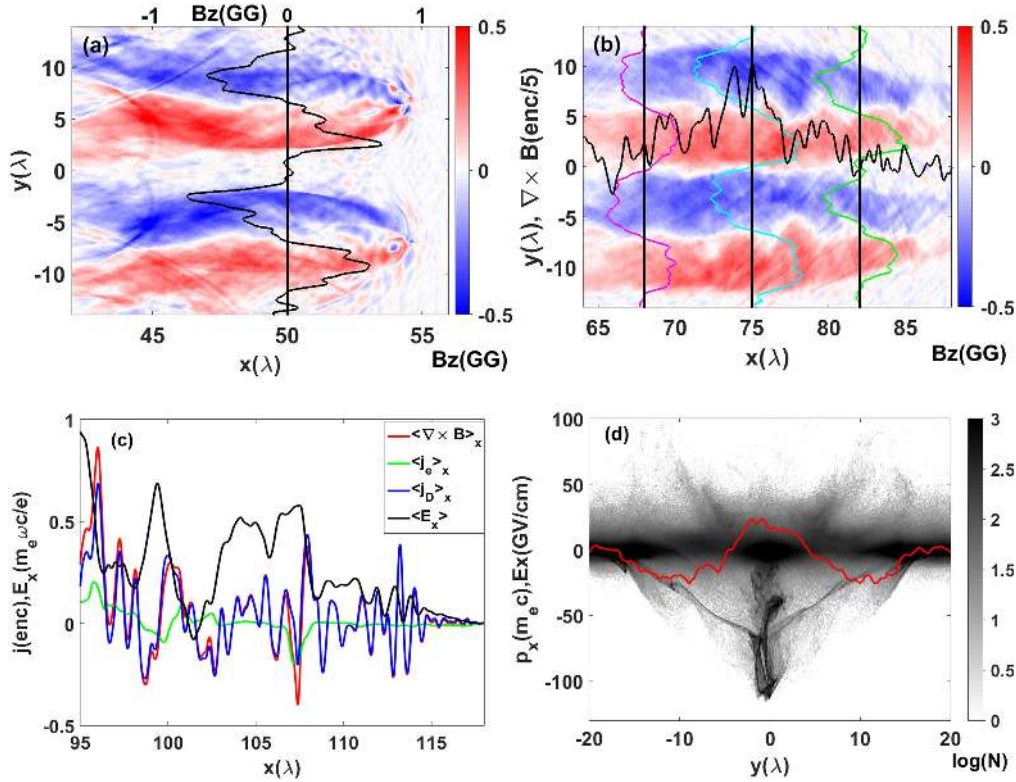
3

Figure 2. (a) The distribution of B_z at $t = 66\,T_0$. The solid black curve is the profile of B_z along $x = 50\,\lambda$ and the dashed line indicates the zero-scale line ($B_z = 0$), which are corresponding to the scale on the upper x-axis. (b) The distribution of B_z at $t = 104\,T_0$. The magenta, cyan and green curves represent the B_z profile along $x = 67\,\lambda$, $75\,\lambda$ and $82\,\lambda$, respectively. The dashed lines are the zero-scale lines for the corresponding locations. The amplitude of the magnetic fields are scaled as same as that in (a). The solid black curve is $(\nabla \times \mathbf{B})_x$ normalized by $enc/5$ along $y = 0$. (c) Contributions of different terms in Ampère–Maxwell law at $128\,T_0$ along $y = 0$, transversely averaged inside the current sheet ($-\lambda < y < \lambda$). The solid red curve is the x-component of $\nabla \times \mathbf{B}$ along $y = 0$. The green and blue lines are the electric current and displacement current, respectively. $\langle \nabla \times \mathbf{B} \rangle_x$, $\langle j_e \rangle_x$ and $\langle j_D \rangle_x$ are normalized to enc. The black curve is the longitudinal electric field normalized to $m_e \omega c/e$. (d) is (y, p_x) phase space plane of the electrons along y-direction at $140\,T_0$. The red line is the longitudinal electric field along $x = 84\lambda$.

downramp region. The transverse expansion is driven by the force proportional to the density gradient ∇n [38, 39]. As a result, the magnetic field covers a wider area while its strength becomes weaker. Figure 2(b) presents the magnetic field distribution in the density downramp region, in which the magnetic dipolar regions touch each other in the center as a result of transverse expanding. The magenta, cyan and green curves are the profiles of B_z along different locations, in which the gradient around the center reflects the variation of magnetic field. The black curve is the x-component of the curl of the magnetic field, $(\nabla \times \mathbf{B})_x$, along $y = 0$. On the head of the channel ($x > 80\lambda$), where the magnetic dipolar regions are not overlapping, the amplitude of $(\nabla \times \mathbf{B})_x$ is negligible. In the channel region, the large amplitude indicates that the magnetic field varies quickly, which also corresponds to the large gradient of the cyan curve ($x = 75\lambda$). The overlap of the magnetic fields with opposite direction induces the magnetic annihilation in 2D and the magnetic reconnection in 3D geometry. Magnetic annihilation is an important part of magnetic reconnection process providing the magnetic field transformation to the electric field. In the 2D case, the magnetic field lines are out of the simulation plane and only the z-components are considered. Therefore it is called magnetic annihilation. In the 3D case, the whole geometry is

modeled and the annihilation of the magnetic field is accompanied with the reconnection.

From equation (3), we see that the variation of the magnetic field is determined by the sum of the conduction current and the displacement current. The contribution from $\mathbf{j} = en\mathbf{v}$, where $\mathbf{v}$ is the electron velocity, is limited by the local electric current density. In our case, due to the downramp density distribution, the local plasma density is low in the region of magnetic annihilation. The maximum of the electron velocity is given by c in the relativistic regime. Therefore the electric current alone cannot compensate the variation of magnetic field. As a result, a large displacement current is induced. Figure 2(c) shows the contributions from each of the components in the Ampère–Maxwell law along the line $y = 0$ at $t = 128\,T_0$. It is close to the end of the target ($x_{max} = 110\lambda$) and the local density is about 10% of the peak density. The electric current density (green) is negligibly small. The curl of magnetic field $\langle \nabla \times \mathbf{B} \rangle$ (red) is only balanced by the displacement current (blue). The displacement current, $\mathbf{J}_D = \partial_t \mathbf{E}$, is the growth rate of an induced electric field. Therefore, a strong longitudinal electric field is generated during the magnetic annihilation process as it is shown by the black curve in figure 2(c). The strength of the electric field reaches several tens GV cm^{-1}. The electric field
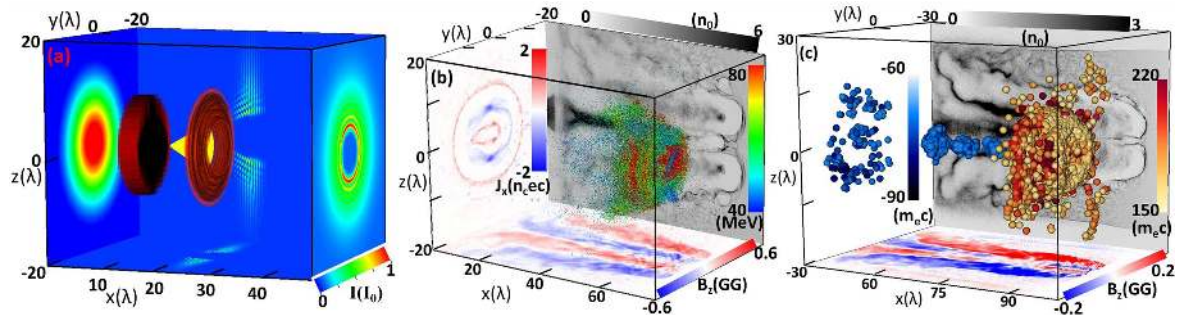
Figure 3. (a) Presents the laser intensity distribution in the 3D case. The cross sections are chosen at $x = 8\,\lambda$ and $23\,\lambda$ at $20\,T_0$, and $35\,T_0$, which are projected on the $x = 0$ and $x = 50\,\lambda$ plane, respectively. The red volume represent the pulse shapes before and after splitting. The split laser intensity in $z = 0$ and $y = 0$ planes are projected in the bottom and the $x = -20\,\lambda$ plane. (b) is the plasma channel structure, the energetic particle distribution, the magnetic field slice and the current slice at $85\,T_0$. (c) Shows the backward accelerated electrons in black–blue spots and the forward energetic particles in yellow–red spots at $110\,T_0$. The corresponding magnetic field distribution and electron density distribution are also included.

accelerates electrons in the direction opposite to the laser pulse propagation direction creating a high energy return current. Via the induced electric field, the magnetic energy dissipates into the kinetic energy of the charged particles. Figure 2(d) presents the phase space of the electrons. The high energy flow of return electrons focuses in the center region, where the magnetic annihilation occurs and where the induced electric field is created. The distribution of the electric field along the y-coordinate is shown by the red curve, in which the maximum part is also located in the center. The backward moving electrons are accelerated up to several tens of MeV.

5. Donut shape pulse in 3D geometry

In order to validate the findings reported in the previous section, we performed 3D PIC simulations of the interaction of an intense laser pulse with the solid density cone followed by an NCD gas jet. The mesh size in this case was $\delta x = \delta y = \delta z = \lambda/15$, which is larger than in the 2D case due to the limitations imposed by computationally demanding simulations in 3D. The number of particles per cell was equal to 12. The cone was placed in the region of $15 < x(\lambda) < 22$ with a radius of 4λ and the same density as in the 2D case ($N = 30\,n_c$). Instead of forming two identical pulses, the laser pulse after the interaction with the cone target transforms into a donut shaped pulse. As noticed in [40], a donut shaped laser has advantages in focusing and accelerating of charged particles. In our case, due to the linear polarization of the laser radiation, the interaction with the cone target leads to the asymmetric pattern of the EM field. The donut shaped pulse is shown in figure 3(a) in a 3D plot. A typical Gaussian distribution of the laser intensity before the splitting is projected on the plane of $x = 0$. The laser pulse shape at $20\,T_0$ and $35\,T_0$ are shown as red disks. We see that the pulse is transformed by the yellow cone target. The intensity distribution after splitting in the x–z plane and x–y plane are projected onto the bottom and the $y = -20\,\lambda$ planes, respectively. The projection of laser intensity in the y–z plane at $x = 23\,\lambda$ and $35\,T_0$, showing the asymmetry in the laser

field distribution, is traced for the sake of readability as a plane at $x = 50\,\lambda$.

The plasma channel formation, the electron beam acceleration, and the corresponding magnetic fields distribution at $85\,T_0$ are shown in figure 3(b). The scatters represent the high energy electrons. The forward accelerated electrons and the electrons moving backwards form the loop structures of the electric currents. The electric current distribution in the cross section at $x = 45\,\lambda$ is projected on the plane of $x = 0$. The channels and the trapped electron beams can be seen in the electron density distribution on the $y = -20\,\lambda$ plane. The bottom plane is the magnetic dipolar regions formed by the electric currents. The dipolar regions represent the distribution of the z-component of the magnetic fields in the $z = 0$ plane, in which the magnetic fields with opposite directions are approaching to each other at this moment.

As we discussed in the 2D simulation case, the displacement current during the magnetic field annihilation generates an induced electric field and accelerates the electrons inside the current sheets. In figure 3(c), the yellow–red spots show the forward moving electrons and the blue–black spots shown the backward accelerated ones. It can be clearly seen that the energetic backward moving electrons are focused in the center region and form a strong return electric current. The magnetic distribution in the bottom plane also shows that the magnetic dipolar regions break in the center, which means the magnetic field is reconnected and the magnetic energy is converted into the particle kinetic energy.

6. Conclusions

In conclusion, we demonstrated an approach towards controlling the relativistic magnetic reconnection by using a solid cone target to split the laser pulse. Accelerated electron beams are generated in the subsequent gas jet plasma, which results in the formation of strong magnetic fields. In both 2D and 3D PIC simulations, high energy backward moving electrons form thin current sheets which are typical for magnetic reconnection. It was also demonstrated that the magnetic field energy can be converted into particle kinetic energy via the

displacement current and the growth of the induced electric field. The energy of accelerated electrons reaches hundreds of MeV. Although it is lower than the electron energy gain in other regimes (e.g. LWFA), it is an important signature of magnetic reconnection. The utilization of a solid cone target enables perfect synchronization of the generated EM pulses, which is a prerequisite for realization of the magnetic reconnection studies at the upcoming laser facilities [41].

Acknowledgments

ORCID iDs

Y J Gu https://orcid.org/0000-0002-6234-8489

References

[1] Biskamp D 1986 *Phys. Fluids* **29** 1520
[2] Berezinskii V S, Bulanov S V, Ginzburg V L, Dogiel V A and Ptuskin V S 1990 *Astrophysics of Cosmic Rays* (Amsterdam: Elsevier Science Publ.)
[3] Biskamp D 2000 *Magnetic Reonnections in Plasmas* (Cambridge: Cambridge University Press)
[4] Yamada M, Kulsrud R and Ji H 2010 *Rev. Mod. Phys.* **82** 603
[5] Bulanov S V 2017 *Plasma Phys. Control. Fusion* **59** 014029
[6] Parker E N 1957 *J. Geophys. Res.* **62** 509
[7] Lin R P *et al* 2003 *Astrophys. J. Lett.* **595** L69
[8] Su Y, Veronig A M, Holman G D, Dennis B R, Wang T J, Temmer M and Gan W Q 2013 *Nat. Phys* **9** 489
[9] Jiong Q, Haimin W, Cheng C Z and Dale E G 2004 *Astrophys. J.* **604** 900
[10] Fermo R L, Opher M and Drake J F 2014 *Phys. Rev. Lett.* **113** 031101
[11] Coppi B, Laval G and Pellat R 1966 *Phys. Rev. Lett.* **16** 1207
[12] Brady P, Ditmire T, Horton W, Mays M L and Zakharov Y 2009 *Phys. Plasmas* **16** 043112
[13] Faganello M, Califano F, Pegoraro F, Andreussi T and Benkadda S 2012 *Plasma Phys. Control. Fusion* **54** 124037
[14] Giannios D 2010 *Mon. Not. R. Astron. Soc. Lett.* **408** L46
[15] Bing Z and Huirong Y 2011 *Astrophys. J.* **726** 90
[16] McKinney J C and Uzdensky D A 2012 *Mon. Not. R. Astron. Soc.* **419** 573
[17] Benot C, Dmitri A U and Mitchell C B 2012 *Astrophys. J.* **746** 148
[18] Furth H P, Killeen J and Rosenbluth M N 1963 *Phys. Fluids* **6** 459
[19] White R 1989 *Theory of Tokamak Plasmas* (Somerset: Elsevier Science)
[20] Yamada M, Levinton F M, Pomphrey N, Budny R, Manickam J and Nagayama Y 1994 *Phys. Plasmas* **1** 3269
[21] Hastie R J 1997 *Astrophys. Space Sci.* **256** 177
[22] Askaryan G A, Bulanov S V, Pegoraro F and Pukhov A M 1995 *Comments Plasma Phys. Control. Fusion* **17** 35
[23] Nilson P M *et al* 2006 *Phys. Rev. Lett.* **97** 255001
[24] Li C K, Seguin F H, Frenje J A, Rygg J R, Petrasso R D, Town R P J, Landen O L, Knauer J P and Smalyuk V A 2007 *Phys. Rev. Lett.* **99** 055001
[25] Dong Q-L *et al* 2012 *Phys. Rev. Lett.* **108** 215001
[26] Rosenberg M J, Li C K, Fox W, Igumenshchev I, Seguin F H, Town R P J, Frenje J A, Stoeckl C, Glebov V and Petrasso R D 2015 *Nat. Commun.* **6** 6190
[27] Wang Y Y, Li F Y, Chen M, Weng S M, Lu Q M, Dong Q L, Sheng Z M and Zhang J 2017 *Sci. China—Phys. Mech. Astron.* **60** 115211
[28] Zhong J *et al* 2010 *Nat. Phys.* **6** 984
[29] Syrovatskii S I 1966 *Sov. Astron.* **10** 270
[30] Gu Y J, Klimo O, Kumar D, Liu Y, Singh S K, Esirkepov T Z, Bulanov S V, Weber S and Korn G 2016 *Phys. Rev. E* **93** 013203
[31] Gu Y J, Klimo O, Kumar D, Bulanov S V, Esirkepov T Z, Weber S and Korn G 2015 *Phys. Plasmas* **22** 103113
[32] Gu Y J, Yu Q, Klimo O, Esirkepov T Z, Bulanov S V, Weber S and Korn G 2016 *High Power Laser Sci. Eng.* **4** E19
[33] Yi L, Shen B, Pukhov A and Fülöp T 2017 arXiv:1708.07676
[34] Ridgers C, Kirk J, Duclous R, Blackburn T, Brady C, Bennett K, Arber T and Bell A 2014 *J. Comput. Phys.* **260** 273
[35] Arber T D *et al* 2015 *Plasma Phys. Control. Fusion* **57** 113001
[36] Bulanov S S, Esarey E, Schroeder C B, Leemans W P, Bulanov S V, Margarone D, Korn G and Haberer T 2015 *Phys. Rev. ST Accel. Beams* **18** 061302
[37] Bulanov S V, Esirkepov T Z, Hayashi Y, Kiriyama H, Koga J K, Kotaki H, Mori M and Kando M 2016 *J. Plasma Phys.* **82** 905820308
[38] Nycander J and Isichenko M B 1990 *Phys. Fluids B* **2** 2042
[39] Yadav S K, Das A and Kaw P 2008 *Phys. Plasmas* **15** 062308
[40] Vieira J and Mendonça J T 2014 *Phys. Rev. Lett.* **112** 215001
[41] Mourou G, Korn G, Sandner W and Collier J 2011 *ELI Extreme Light Infrastructure (Whitebook)* (Berlin, Germany: THOSS Media GmbH)